

STATISTICAL CHARACTERISTICS OF THE INTERACTION OF AN IMPINGING SHOCK WAVE AND TURBULENT BOUNDARY LAYER

M. F. Shahab, G. Lehnasch, T. B. Gatski and P. Comte

Laboratoire d'Études Aérodynamiques (LEA)

Université de Poitiers, ENSMA, CNRS

43 Rue de l'Aérodrome, 86036 Poitiers cedex, France

muhammad.shahab@ceat.univ-poitiers.fr

ABSTRACT

A spatially evolving, supersonic boundary layer flow with an impinging shock has been computed using direct numerical simulation. The free stream Mach number M_∞ is 2.25 and the momentum thickness Reynolds number (based on free stream conditions) Re_θ is 4000. The same turbulent flow but without the impinging shock is the comparison basis that provides a gauge to assess the extent by which the turbulent statistical moments are altered due to the presence of the shock. In this impinging shock study, some scalar fluxes and velocity second- and higher-order moments are monitored and assessed at several stations along the plate so that the effect of the shock can be assessed both upstream, downstream and in close streamwise proximity to the impingement point.

INTRODUCTION

For wall bounded flows, the effect of the shock can induce flow separation that can be either open or followed by a reattachment region. It opens the possibility for different modes of instability so that most of the wall-bounded shock wave interacting flows are subject to low frequency instabilities. The problem is truly three-dimensional with the issue of shock oscillation an important factor in the dynamics. Without shock impingement and at a range of supersonic Mach numbers of 2.25 and above, the compressible flow field variables satisfy the same similarity relationships as their incompressible counterparts when fluid property variations across the flat plate boundary layer are taken into account.

There is an abundance of mean and turbulent correlations that can be used to verify supersonic boundary layer flow simulations without shocks. Using the van Driest transformation as well as applying the various forms of the (extended) strong Reynolds analogies provides an ample set of verification measures. With shocks, the verification procedures and assessment of simulation quality is less direct. The simulations are complicated by the interactions between the shock and the turbulent field. In the inner layer region, the shock can induce separation and reattachment along the solid boundary, and in the outer layer region the shock amplifies the turbulent field. In addition, the turbulent field and the separation zone can induce a coupled unsteadiness in the motion of the shock.

Some of these statistical correlations for both the thermal and velocity fields in the vicinity of the shock impingement point and separation bubble are further investigated here.

NUMERICAL PROCEDURE AND PHYSICAL DOMAIN

In performing numerical simulations of such wall bounded flows, two main types of strategies are possible.

One is based on the simulation of a developing turbulent flow field and the other is based on the simulation within a subset domain where the turbulent flow field is sustained through either a recycling/rescaling procedure (e.g. Stolz and Adams, 2003) or a specification of inflow conditions (see e.g. Martin, 2007). The approach here is to perform a simulation corresponding to the former case where the flow is allowed to develop from the laminar, through the transitional and into the fully turbulent regime. While this increases the number of grid points required relative to the latter case where only a fully turbulent regime is considered, it precludes any potential for adversely affecting the unsteady motion of the shock.

For the numerical procedure, the compressible Navier-Stokes equations, in its conservation form, are discretized. An efficient high-order hybrid compact WENO algorithm is used that includes a seventh-order scheme based on the Lax-Friedrich reconstruction method for the inviscid terms (Shu, 1997) and a fourth-order compact scheme for the viscous terms. The temporal integration is performed by means of four-stage fourth-order non-TVD Runge-Kutta scheme.

Although the full streamwise extent of the computational domain includes a transitional flow regime, the focus here is on a more limited domain in the fully turbulent region as shown in Fig. 1. Data in a series of $y-z$ planes at different

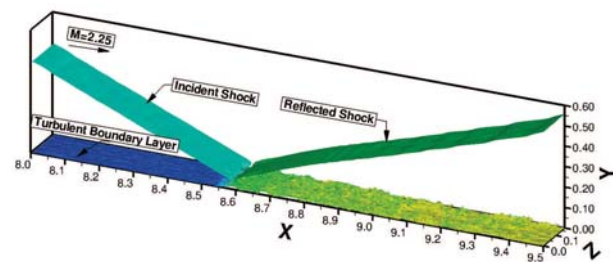


Figure 1: Overview of computational sub-domain in vicinity of the incident/reflected shock intersection. (Shading based on pressure level.)

streamwise stations have been analyzed with a focus towards a mapping of the statistical correlations in the vicinity of the shock impingement region. Figure 2 shows a mapping of these locations relative to the separation bubble induced by the shock impingement. The corresponding locations are also tabulated and shown in Table 1. It should be noted that the shock oscillates due to the interaction with the turbulence so the values shown are mean values obtained by both time averaging and averaging in the z -direction (the turbulence is assumed homogeneous in this direction and periodic boundary conditions are applied).

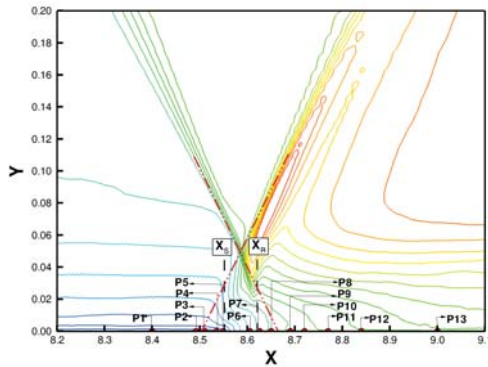


Figure 2: Streamwise location of $y - z$ planes in proximity of separation bubble.

Table 1: Locations of diagnostic planes relative to separation and reattachment points.

Plane	x -pos.	Plane	x -pos.
1	8.399	7	8.624
2	8.490	8	8.649
3	8.509	9	8.689
4	8.534	10	8.718
5	8.548	11	8.768
Sep. Pt.	8.549	12	8.839
6	8.604	13	8.998
Reatt. Pt.	8.621	14	9.779

INFLUENCE OF SCALAR FLUXES

In the absence of shocks or imposed mean thermal gradients, the influence of the scalar fluxes on the mean and turbulent velocity fields is minimal. However, in flow fields where shocks are present, the influence of heat and mass flux correlations can be significant and can be important contributors to the dynamic balance in the respective transport equations.

Mass Flux

The mass flux terms are associated with fluctuating density correlations and appear in the turbulent stress transport equations involving the mean pressure gradient and mean viscous stress gradient. In addition, these terms also provide a link between the density-weighted variables and the Reynolds-averaged variables in RANS type calculations. This latter appearance of the mass flux is relevant to cases where results from simulations and computations are compared to experimental results. Of course, a fundamental question when assessing and comparing data is whether the comparisons are with the same variables. It has been found that at supersonic speeds under adiabatic conditions (without shocks), the mass flux terms are not significant so that experimentally measured Reynolds variables and numerically obtained density-weighted variables differ little. At hypersonic speeds, the situation may differ, but there has not been enough (direct) numerical simulations to adequately address this issue (e.g. Maeder et al., 2001; Martin, 2007). However, in the presence of shocks even at supersonic speeds, the mass flux can be significant and so quantitative comparisons with experiments need to be performed more cautiously. The following serves to illustrate the effect of shocks on these fluctuating density correlations.

The relationship between the density-weighted (Favre) averaged turbulent velocity second moments and the Reynolds averaged correlations is

$$\overline{u_i'' u_j''} = \overline{u_i' u_j'} + \frac{\overline{\rho' u_i' u_j'}}{\overline{\rho}} - \frac{(\overline{\rho' u_i'}) (\overline{\rho' u_j'})}{\overline{\rho}^2}, \quad (1)$$

with the corresponding anisotropy tensors being given by

$$\tilde{b}_{ij} = \frac{\overline{u_i'' u_j''}}{\overline{u_i' u_i'}} - \frac{\delta_{ij}}{3} \quad \text{and} \quad \bar{b}_{ij} = \frac{\overline{u_i' u_j'}}{\overline{u_i' u_i'}} - \frac{\delta_{ij}}{3}. \quad (2)$$

An example of the effect an impinging shock has on the different turbulent correlations can be seen from a comparison of the distribution of the turbulent stresses across the layer at two different streamwise locations along the flat plate boundary layer. Figure 3 shows the distribution at the location P4 (see Fig. 2 and Table 1) along the plate. As Table 1 indicates, this is a point upstream of the (averaged) boundary layer separation point. (In the figures, the boundary layer scaling used δ is the boundary layer thickness at the inviscid impingement point ($x = 8.676$), $\delta = 0.08027$). The comparison indicates that except for the shear stress component, the difference between the two types of second-moments is generally less than 5%. For the shear stress component, there is a region near the boundary layer edge where the difference is almost 25% between the Favre and Reynolds averaged shear stress component ($0.75 \lesssim y/\delta \lesssim 1.0$). A comparison with Fig. 2 shows that this region where the shear stress components differ corresponds to the intersection of the plane P4 with the incident shock, $y/\delta \approx 0.94$.

A similar qualitative, though different quantitative, result is found farther downstream at the plane P6 which is located at a streamwise station that lies between the boundary layer separation and reattachment points (see Table 1). Figure 4 shows that once again the shear stress component and the associated mass flux terms have a significant influence on the turbulence dynamics. Although the magnitude of the turbulent shear stress ratio may be adversely affected by the deterioration of numerical accuracy in this narrow region, the qualitative behavior is clear and occurs in a region where the plane P6 intersects the incoming shock at $y/\delta \approx 0.45$. Although the quantitative influence is different, Figs. 3 and 4 both show that the mass flux can have a significant affect on the turbulence statistics; although, the effect is localized to the (important) shear stress component.

The inherent complexity of compressible flow dynamics is illustrated here by considering the corresponding invariant map associated with the turbulent stress anisotropy field at plane P6. This representation of the turbulence field based on this componentality of the turbulent stress anisotropy (defined in Eq. (2)) yields a surprising picture at first glance. Figure 5 shows the behavior of the anisotropy tensor corresponding to both density-weighted variables \tilde{b}_{ij} and Reynolds averaged variables \bar{b}_{ij} position plane P6. For clarity of presentation, only the invariants lying in the range $0.2 < y/\delta < 0.45$ are shown. The figure shows that the invariants extracted from both types of averaged turbulent stresses yield similar qualitative (and to a slightly less quantitative) picture. In both cases, the invariant map shows that the turbulence is dominated by a single stress component (b_{11}) and along this axisymmetric boundary, the shear stress component has a minimal effect on the turbulent dynamics (Simonsen and Krogstad, 2005). Thus, while Fig. 4 suggests an important role for the shear stress and associated mass flux terms, it turns out from a dynamical

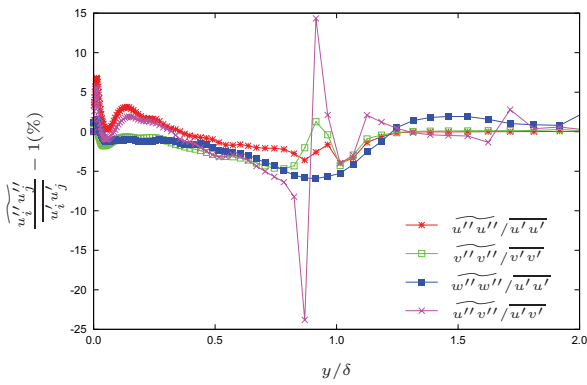


Figure 3: Normalized turbulent stresses at plane P4 upstream of boundary layer separation point.

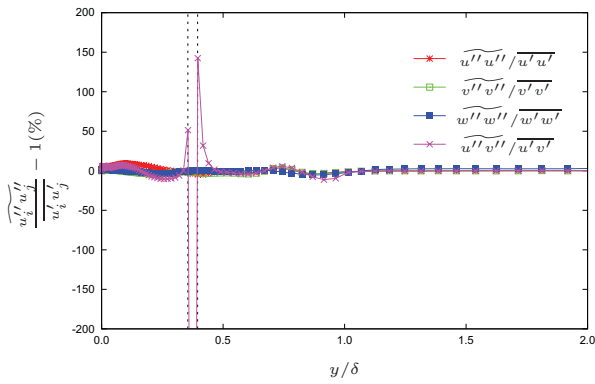


Figure 4: Normalized turbulent stresses at plane P6 between boundary layer separation and reattachment point.

standpoint this otherwise important turbulent stress component has minimal effect. An analysis of the simulation data shows that in this region, the magnitude of the b_{12} is an order of magnitude smaller than the corresponding normal stress anisotropy components. It should be recalled that in direct simulations (Mahesh et al., 1997; Jamme et al., 2002) of homogeneous turbulence interacting with a normal shock, that downstream of the shock the streamwise component of the normal turbulent stresses is more strongly amplified than the other two components. Such a normal stress distribution is consistent with the axisymmetric boundary on the right side of the invariant triangle.

Heat Flux

As the previous section has shown, the correlations associated with the density fluctuations have a significant effect on the averaging process for the turbulent velocity correlations in the vicinity of the shock. This suggests that a similar effect will surface for other quantities such as the heat flux correlation. Analogous to the velocity correlation relationship given in Eq. (1), the relationship between the density-weighted (Favre) averaged and the Reynolds averaged heat flux vectors can be written as

$$\overline{u_i''T''} = \overline{u_i'T'} + \frac{\overline{\rho'u_i'T'}}{\bar{\rho}} - \frac{(\overline{\rho'u_i'}) (\overline{\rho'T'})}{\bar{\rho}^2}, \quad (3)$$

Although similar in form to the velocity correlations in the previous section, Eq. (3) is implicitly more complex since the density field is dependent on the temperature field.

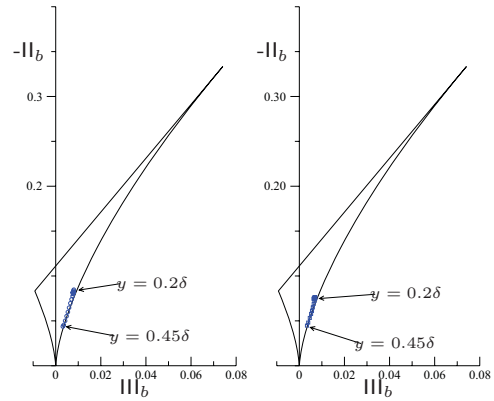


Figure 5: Invariant mapping of turbulent stress anisotropy at plane position P6: Left, Favre average \circ ; Right, Reynolds average \square .

Figure 6 shows the heat flux distributions at the streamwise location P4 (see Fig. 2 and Table 1) along the plate. The influence of the shock on the averaging procedure used in obtaining the streamwise heat flux component is negligible; whereas, the effect on the cross-stream flux is significant and extends well outside the boundary layer. (It should be cautioned that the grid resolution outside the boundary layer deteriorates so that magnitude levels may be suspect in this region.) Near the wall, the cross-stream heat flux also shows a large difference between the two averaging procedures. Since in this region the numerical accuracy should be sufficient, both the qualitative and quantitative effects need to be considered. The origin of this near wall behavior is not clear at this point and will require further investigation.

At location plane P6 shown in Fig. 7, the cross-stream scalar flux is once again influenced by the incoming shock at $y \approx 0.45$ (cf. Fig. 3 and Fig. 4). Near the wall, both scalar fluxes show large differences between the two averaging procedures suggesting a strong effect from the density fluctuation correlations. Since plane P6 is located within the separation bubble the dynamics is complex and, of course, further complicated by the dependence of the density fluctuations on the temperature field.

EFFECT ON SECOND AND HIGHER-ORDER MOMENTS

Since it is not possible here to analyze all the various statistical moments involving the fluctuating velocity field, it is of useful, nevertheless, to examine the behavior of some quantities that are of relevance in understanding the dynamics of shock impinging flows. With this motivation, the streamwise behavior of the stress anisotropy tensor is examined as well as the influence of the transport and baroclinic terms that appear in the solenoidal dissipation rate equation. Finally, a comparison of simulation skewness and flatness (kurtosis) data with experiments is made and evaluated.

Turbulent Stress Anisotropy

Figure 8 shows the streamwise variation of the density-weighted turbulent stress anisotropy at two location, $y/\delta = 0.0027$ and $y/\delta = 0.047$, within the boundary layer. Two distinct regions are identified. At $y/\delta = 0.0027$, it is seen that as the separation bubble is approached the invariant points (P1, P4, P6) move along the two-component limit

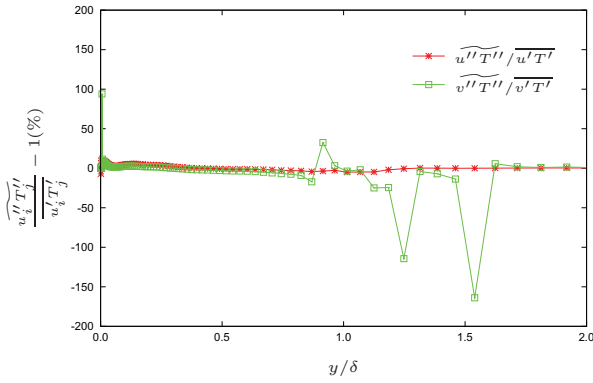


Figure 6: Normalized turbulent heat fluxes at plane P4 upstream of boundary layer separation point.

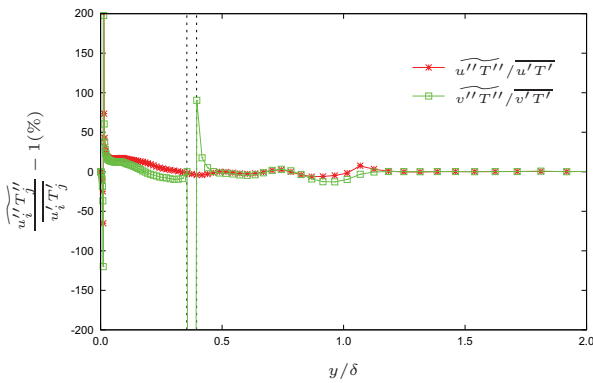


Figure 7: Normalized turbulent heat fluxes at plane P6 between boundary layer separation and reattachment point.

boundary toward the two-component axisymmetric boundary. Even after the separation point at location P10, the invariant point is still located at the two-component axisymmetric boundary. Only after some distance downstream (P14), where the flow is sufficiently relaxed back to its pre-distortion state, does the invariant map show the behavior as at location P1. As Figure 8 shows, at $y/\delta = 0.047$ the invariant map has a different characteristic behavior. It is interesting to note at first that the points corresponding to locations P1 and P14 are not as close as they were at $y/\delta = 0.0027$. This suggests that as one moves farther from the wall, the relaxation process requires more distance downstream from the distortion. In general, as the separation bubble is approached the trend is along the axisymmetric boundary and towards the isotropic limit. Somewhat surprisingly, the point corresponding to location P10 is relatively close to the isotropic limit even though the direct affect of the impinging shock has occurred upstream of this location.

Compressible Transport and Baroclinic Terms

The role of the turbulent kinetic energy dissipation rate has long been a subject of study in compressible flow fields. In the absence of shocks, the solenoidal dissipation rate has been found to dominate over any dilatational dissipation rate effects. The corresponding solenoidal dissipation rate has been analyzed (e.g. Kreuzinger et al. 2006) and terms due solely to compressibility effects have been identified, and included a compressible turbulent transport term, a baroclinic

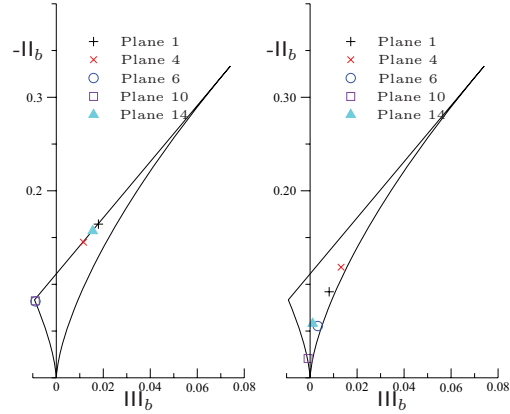


Figure 8: Invariant mapping of turbulent stress anisotropy at a fixed y/δ location: Left $y/\delta = 0.0027$; Right $y/\delta = 0.047$.

term, and a term associated with the viscous stress gradient. Of these three, the first two were shown to dominate in *a priori* tests using numerical simulation data. The transport and baroclinic terms can be written as

$$T_\epsilon^c = \bar{\nu}(u'_{i,j} - u'_{j,i})u'_{i,j}u'_{k,k}, \tag{4}$$

and

$$B_\epsilon = 2\bar{\nu}(u'_{i,j} - u'_{j,i})\rho_{,j}p_{,i}/\rho^2, \tag{5}$$

respectively. Figures 9 and 10 show the distribution of these two terms at a variety of streamwise stations along the plate. Transport effects are clearly confined to the very near wall region; although at plane P6, which is within the separation bubble, the magnitude of the term increases relative to the values at the other stations. The influence of the baroclinic term extends a little farther into the boundary layer relative to the transport term, but is still confined to the near wall region. An interesting trend is that the magnitude of the baroclinic term at plane 4 exceeds that at plane 6, and is not impacted (at either location) with a direct effect of the impinging shock. Of course a more thorough analysis is needed particularly a term by term comparison with other terms in the solenoidal dissipation rate equation in order to determine the relative importance of the baroclinic term itself. Nevertheless, from Figs. 9 and 10 it is possible to conclude of the three compressible terms that in the solenoidal equation only the baroclinic term will need to be considered and eventually modeled.

Skewness and Flatness

Since the focus here has been on the statistical moments, it is natural to examine some higher-order moments that can provide some information about the associated probability density function (pdf). These two higher-order moments are the skewness and flatness (kurtosis) factors defined by

$$S(u'_i) = \frac{\overline{u_i'^3}}{(\overline{u_i'^2})^{3/2}}, \quad F(u'_i) = \frac{\overline{u_i'^4}}{(\overline{u_i'^2})^2} \tag{6}$$

where $i = 1, 2, 3$ (no summation). The skewness is associated with the asymmetry of the tails of the pdf function, and the flatness is a relative measure of the weight in the tails of the distribution. In both cases the basis of comparison is the Gaussian distribution with zero skewness and a flatness factor of three. Figures 11 and 12 show variation of these

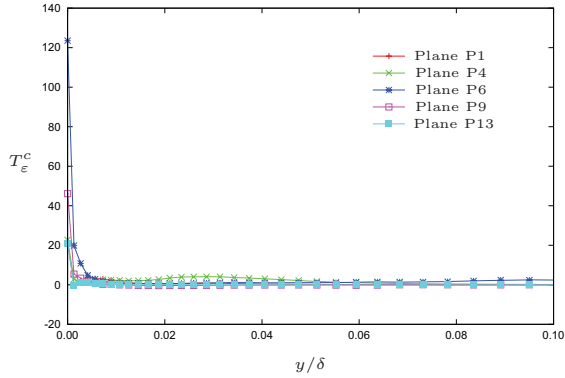


Figure 9: Distribution of transport term T_ϵ^c in near wall region at different streamwise stations.

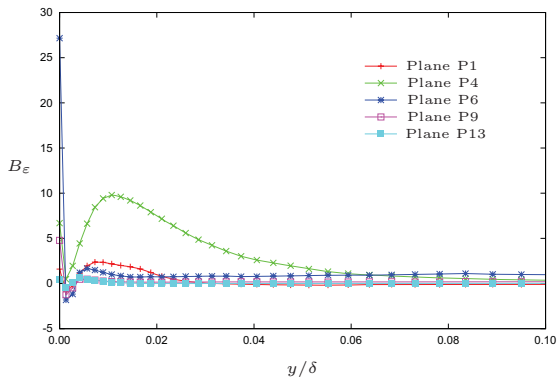


Figure 10: Distribution of baroclinic term B_ϵ in near wall region at different streamwise stations.

quantities across the boundary layer at different streamwise stations. In addition, the numerical simulation data is compared to the experimental results of Deleuze (1995) at two stations. (Note that the upstream location of the experimental data does not correspond to the plane P1 of the simulation, but is farther upstream. Nevertheless, in both cases the skewness and flatness data is not influenced by the incoming shock. The downstream location of the experimental data does correspond to the location of plane P12.) As the figure shows, the skewness distribution upstream of the shock for both the simulation (P1) and experimental (upstream) data show the expected boundary layer behavior of positive values very near the wall and negative values away from the wall. Away from the shock distortion region, the simulation (P12) and experimental (downstream) data have a similar qualitative behavior which, however, differs from the pre-distortion data upstream. This is not surprising since the other statistical quantities examined also suggest that at these downstream stations the flow has not relaxed back from the effects of the impinging shock. The skewness at the location plane P6 which is located between the boundary layer separation and reattachment points is not affected as much as might be expected.

In Fig. 12 a similar comparison is shown for the flatness factor. The simulation data at all planes (P1, P6, P12) shows a peak value at the wall suggesting strongly intermittent turbulence. Away from the wall, the simulation data at planes P1 and P6 remain near 3, but the downstream station P12 shows a generally higher value across most of the layer. Near the boundary layer edge, the upstream simulation (P1)

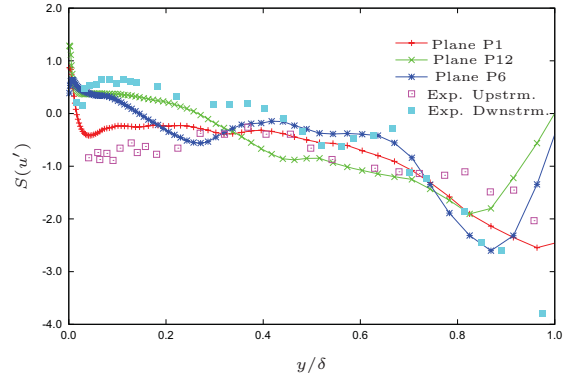


Figure 11: Comparison of experimental (Deleuze, 1995) and simulation streamwise velocity skewness data within boundary layer.

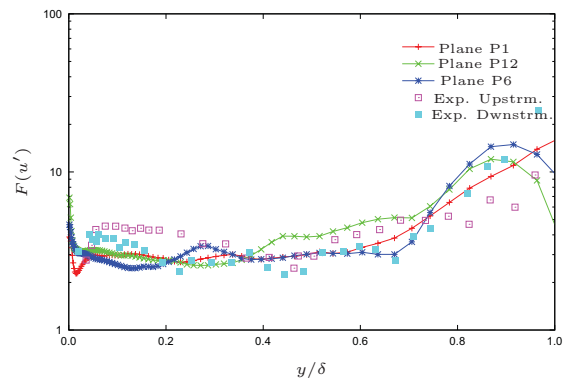


Figure 12: Comparison of experimental (Deleuze, 1995) and simulation streamwise velocity kurtosis data within boundary layer.

and experimental (upstream) data show an increase in value indicating the increase in intermittency; however, at locations P6 and P12 there is a decrease. Further investigation is needed to better understand this behavior.

The flatness factor also plays a useful role in assessing the intermittency of the flow. The intermittency factor γ_I can be defined as $3/F$ and it has obtained from both experimental (Eléna and Lacharme, 1988; Deleuze, 1995) and simulation (Martin, 2007) data previously in supersonic boundary layer flows without shocks. The current simulation data at plane P1 can be compared to these other studies in order to validate the upstream simulation data. Figure 13 shows a comparison of the intermittency factor from the present simulation with previous experimental and simulation results. The overall qualitative trend is consistent among the data shown; although, there is general under-prediction of the experimental results relative to the simulation results. Another, more subtle factor, is the rise in intermittency at the outer edge of the boundary in the simulation data of Martin (2007). This simulation (Martin, 2007) utilized a turbulent initialization procedure (sustained turbulence) rather than the developed turbulence procedure used here. Whether this is the origin of the rise in intermittency needs further study.

In Figure 14, the streamwise variation of the intermittency factor is shown. As with the flatness factor plot (Fig. 12), the intermittency factor shown at location plane P12 does not display the same characteristics as the upstream

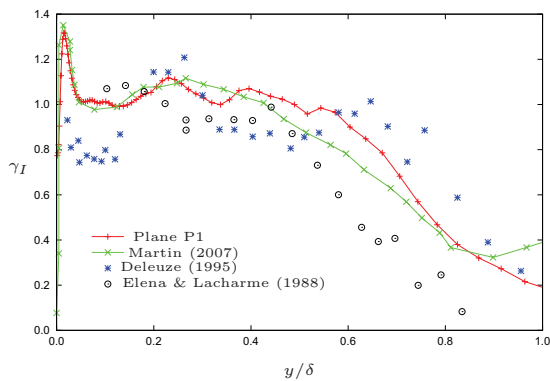


Figure 13: Comparison of experimental and simulation intermittency data within boundary layer upstream of shock interaction zone.

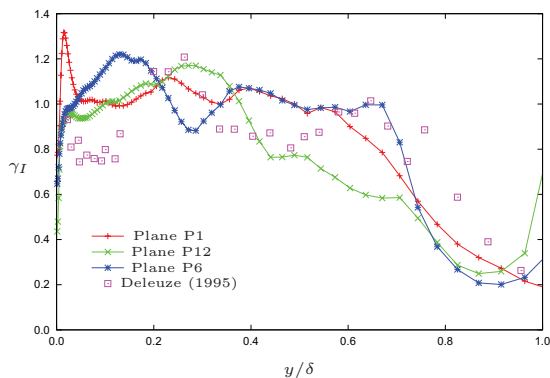


Figure 14: Variation of intermittency data at various stream-wise locations within boundary layer. Experimental data of Deleuze (1995) upstream of interaction zone.

(undistorted) plane P1. This indicates that the turbulent structure has been altered and will apparently remain so for some distance downstream. In addition, the rise in intermittency factor noted in the (without shock) simulation of Martin (2007) now surfaces at the location plane P6 and further downstream at P12. In the near-wall region, a decrease in intermittency is observed a planes P6 and P12 relative to the upstream plane P1.

SUMMARY

Some statistical correlations associated with the thermal and velocity fields have been investigated in order to gain further insight into the effect of an impinging shock on an inhomogeneous (anisotropic) turbulent flow field. It was first shown that the mass flux correlations $\overline{\rho' u_i'}$ and $\overline{\rho' u_i' u_j'}$ can become large in the vicinity of the shock and that correlation involving the cross-stream turbulent velocity fluctuation are mostly affected. This behavior then affects the the type of averaging procedure used so that data comparisons with, for example, experiments need to be done carefully in the vicinity of the shocks. In addition, sudden distortions imposed on turbulent flow fields necessitates the need to take into account a (streamwise) relaxation effect of the turbulence. Such behavior then should be accounted for in the usual computational methods, such as a RANS approach, in order to properly predict the flow field. Of particular interest here, was the effect of the shock induced distortion on the

turbulent statistics. The variation was examined for the turbulent stress anisotropy tensor through the Lumley invariant map, the effect on the turbulent transport term and baroclinic term relevant to the energy dissipation rate dynamics, and finally on the skewness and flatness (kurtosis) factors as well as the related intermittency factor. From these results, the next task is to develop a consistent picture of how such inhomogeneous and anisotropic shock distortions affect the turbulence and then develop a more accurate means of prediction and control.

Acknowledgment: MFS acknowledges the support of the Higher Education Commission Pakistan. The authors gratefully acknowledge the support of the Agence Nationale de la Recherche under the Project SPICEX (ANR-07-CIS7-009) and IDRIS, the CNRS supercomputing center, under Project CP2-90912.

REFERENCES

- Deleuze, J., 1995, "Structure d'Une Couche Limite Turbulente Soumise à Une Onde de Choc Incidente", *Université de la Méditerranée Aix - Marseille*.
- Eléna, M. and Lacharme, J. 1988, "Experimental Study of a Supersonic Turbulent Boundary Layer Using a Laser Doppler Anemometer", *J. Méc. Théor. Appl*, Vol. 7, pp. 175-190.
- Jamme, S., Cazalbou, J.-B., Torres, F., and Chassaing, P., 2002, "Direct Numerical Simulation of the Interaction Between a Shock Wave and Various Types of Isotropic Turbulence", *Flow Turbul. Combust.*, Vol. 68, pp. 227-268.
- Kreuzinger, J., Friedrich, R., and Gatski, T. B., 2006, "Compressibility Effects in the Solenoidal Dissipation Rate Equation: A Priori Assessment and Modeling", *Int. J. Heat Fluid Flow*, Vol. 27, pp. 696-706.
- Maeder, T., Adams, N. A., and Kleiser, L., 2001, "Direct Simulation of Turbulent Supersonic Boundary Layers by an Extended Temporal Approach", *J. Fluid Mech.*, Vol. 429, pp.187-216.
- Mahesh, K., Lele, S. K., and Moin, P., 1997, "The Influence of Entropy Fluctuations on the Interaction of Turbulence with a Shock Wave", *J. Fluid Mech.*, Vol. 334, pp. 353-379.
- Martin, M. P., 2007, "Direct Numerical Simulation of Hypersonic Turbulent Boundary Layers. Part 1. Initialization and Comparison with Experiments", *J. Fluid Mech.*, Vol. 570, pp. 347-364.
- Shu, C.-W., 1997 "Essentially Non-Oscillatory and Weighted Essentially Non-Oscillatory Schemes for Hyperbolic Conservation Laws". *ICASE Report No.97-65*.
- Simonsen, A. J. and Krogstad, P.-Å., 2005, "Turbulent Stress Invariant Analysis: Clarification of Existing Terminology", *Phys. Fluids*, Vol. 17, pp. 088103-1-4.
- Stolz, S. and Adams, N. A., 2003, "Large-Eddy Simulation of High-Reynolds Number Supersonic Boundary Layers Using the Approximate Deconvolution Model and a Rescaling and Recycling Technique", *Phys. Fluids*, Vol. 15, pp. 2398-2412.